Advances in Water Resources 144 (2020) 103697

Contents lists available at ScienceDirect

Advances in Water Resources

journal homepage: www.elsevier.com/locate/advwatres

Impact of phases distribution on mixing and reactions in unsaturated porous media

Joaquín Jiménez-Martínez[a,b,*], Andrés Alcolea[c], Julien A. Straubhaar[d], Philippe Renard[d]

[a] Department of Water Resources and Drinking Water, EAWAG, 8600 Dübendorf, Switzerland
[b] Department of Civil, Environmental and Geomatic Engineering, ETH Zurich, 8093 Zürich, Switzerland
[c] HydroGeoModels AG, Tösstalstrasse 23, 8400 Winterthur, Switzerland
[d] Centre d'Hydrogéologie et de Géothermie (CHYN), University of Neuchâtel, 2000 Neuchâtel, Switzerland

ARTICLE INFO

Keywords:
Phase saturation
Phases distribution
Solute mixing and reactions
Pore scale
Multiple point statistics
Simulation

ABSTRACT

The impact of phases distribution on mixing and reaction is hardly assessable experimentally. We use a multiple point statistical method, which belongs to the family of machine learning algorithms, to generate simulations of phases distributions from data out of laboratory experiments. The simulations honour the saturation of the laboratory experiments, resemble the statistical distributions of several geometric descriptors and respect the physics imposed by capillary forces. The simulated phases distributions are used to compute solute transport. The breakthrough curves reveal that different phases distributions lead to broad ranges of early arrival times and long-term tailings as saturation decreases. For a given saturation, a similar long-term scaling of mixing area, interface length, and corresponding reactivity is observed regardless of phases distribution. However, phases distribution has a clear impact on the final values (before breakthrough) of area of mixing, interface length and mass of reaction product.

1. Introduction

The proper understanding of solute spreading (dispersion), mixing and reaction is key to the success of natural and engineered remediation of pollutants in the subsurface. The characterization of dispersion is important to predict the current or future spatial extent of a contaminant plume. However, dispersion does not provide any information about the mixing of the solute (*i.e.*, the distribution of solute concentration within the plume), which controls chemical reaction processes (Fluhler et al., 1996; Dentz et al., 2011; de Barros et al., 2012; Chiogna et al., 2012; de Anna et al., 2014). In the unsaturated zone, between the soil surface and the groundwater level, all three mechanisms, dispersion, mixing and reaction, depend on saturation (*i.e.*, the fraction of pore volume occupied by water). For instance, an increase in dispersion is observed as saturation decreases, due to the development of high and low velocity regions (respectively, preferential flow paths and stagnation zones; De Gennes, 1983). However, an unexpected decrease of dispersion below a certain threshold, so-called critical saturation, has also been observed (Toride et al., 2003; Raoof and Hassanizadeh 2013). Above the critical saturation, the development of preferential flow paths favours faster travel times leading to shorter times for mixing and reaction (Vanderborght et al., 2001; Ursino et al., 2001; Persson et al., 2005; Gouet-Kaplan and Berkowitz, 2011; Kapetas et al., 2014). In addition, flow channelling may also increase concentration gradients, thus enhancing diffusive mass transfer and reaction rates (Jiménez-Martínez et al., 2015, 2017).

The impact of saturation on transport processes, and in particular on dispersion, has been widely studied at the field scale through displacement experiments in columns using both glass beads or natural soils (De Smedt and Wierenga, 1984; Maraqa et al., 1997; Matsubayashi et al., 1997; Haga et al., 1999; Padilla et al., 1999; Sato et al., 2003; Nutzmann et al., 2002; Toride et al., 2003; Bunsri et al., 2008). More recently, two-dimensional experiments down to pore scale observations have been carried out in heterogeneous media (*e.g.*, Karadimitriu et al., 2016; Jiménez-Martínez et al., 2015, 2017). Such experiments are costly and time-consuming which, together with the difficulties in obtaining equivalent degrees of heterogeneity for a given saturation (and for different saturations), hinders the analysis of the impact of phases distribution on mixing and reaction. This problem can be tackled numerically and is known as image reconstruction. In the context of porous media, a number of methods have been developed to reconstruct aquifer or sample architecture from partial data sets, *e.g.*, the optimization-based method (Yeong et al., 1998), pilot points based methods (Alcolea et al., 2006, 2008), the phase recovery method (Hasanabadi et al., 2016), the Gaussian random fields method (Roberts, 1997), the superdimension method (Rozman and Utz, 2001), cross-correlation-based simulation

* Corresponding author at: Department of Water Resources and Drinking Water, EAWAG, 8600 Dübendorf, Switzerland.
E-mail addresses: joaquin.jimenez@eawag.ch, jjimenez@ethz.ch (J. Jiménez-Martínez).

https://doi.org/10.1016/j.advwatres.2020.103697
Received 2 May 2020; Received in revised form 15 July 2020; Accepted 15 July 2020
Available online 16 July 2020

(Tahmasebi and Sahimi, 2013), supervised learning (Tahmasebi, 2018) and multiple point statistics (Hajizadeh et al., 2011; Comunian et al., 2012; Mariethoz and Renard, 2010). Multiple point statistical (MPS) methods generate equally likely (conditional or unconditional to data) simulations of the patterns captured from a training data set (TDS hereinafter), usually an image representing a "conceptual model" or an analogue to what is being simulated. MPS methods belong to the broad family of machine learning techniques. In fact, it has been recently demonstrated that (1) the traditional MPS methods can be enhanced via deep learning, and (2) that the capabilities of MPS methods for reproducing/reconstructing sophisticated geometries of small scale features and connectivity of complex 3D media is virtually unlimited and only bounded by CPU issues (Feng et al., 2018).

In this work, we address numerically the effect of phases distribution on mixing and reaction by generating MPS equally like simulations of phases distribution that inherit the spatial patterns of a TDS obtained from a laboratory experiment. To that end, we use the MPS method recently devised by Straubhaar et al., 2020. Three different two-dimensional saturation degrees, obtained from previous experiments (Jiménez-Martínez et al., 2017) were used. After prior (merely geometric) evaluation of the reliability of the computed simulations, steady state creeping flow and conservative transport were simulated numerically and derived magnitudes (*e.g.*, breakthrough curves and reaction rates amongst others) were calculated. The comparison of the sets of outputs corresponding to different saturations allowed us to confirm numerically what is already known experimentally about the impact of saturation on solute dispersion, mixing and chemical reactions, *i.e.*, that lower saturation enhances all three mechanisms (Jiménez-Martínez et al., 2015, 2017; Jougnot et al., 2018). This is an independent confirmation of the goodness of the suggested approach that motivates further analyses of the impact of phases distribution on mixing and reaction for a given saturation. To that end, we assume a fast-homogeneous irreversible reaction (*e.g.*, de Simoni et al., 2005, 2007; Willmann et al., 2010) and compute the effective reactivity and the total mass of reaction product from local concentration gradients.

This manuscript is organized as follows. Section 2 summarizes the experimental data sets (*i.e.*, the phases distributions for three given saturation degrees used as TDS), the numerical model adopted for solving creeping flow and conservative solute transport, and the computation of mixing and reaction from the numerically solved concentration fields. In Section 3, we succinctly describe the MPS method used to generate equally likely phases distributions from a given training data set. In Section 4, we present and discuss the results. The paper ends with concluding remarks about the importance of phases distribution on reaction and mixing.

2. Methodology

The proposed methodology consists of three main steps, described in detail in dedicated sub-sections:

- Step 1: laboratory experiment under controlled saturation conditions. The main outcome of the experiment is a high-resolution image depicting the steady state (*i.e.*, final) spatial distribution of air clusters and solid obstacles. The image is the so-called "training data set", TDS.
- Step 2: generation of equally likely MPS simulations inheriting the statistical patterns and mimicking the aforementioned image. A set of geometric and statistical coherence checks is made to warrant that simulated phases distributions analogue to the given TDS.
- Step 3: flow and solute transport simulation and evaluation of derived outcomes, including breakthrough curves, geometry of the mixing zone (area and fluid-fluid interface length), reactivity, and mass of reaction product, to address the impact of phases distributions on dispersion, mixing and reaction.

2.1. Laboratory experiment

The two-dimensional water-wet porous medium under study (132 mm length and 87 mm width) is made of a total of 4421 irregularly distributed circular obstacles, with mean diameter $d = 0.83 \pm 0.22$ mm. These define an average pore size $\lambda = 1.85$ mm and an average pore throat $a = 1.17$ mm, which yield a final porosity $\phi = 0.71$ and permeability $\kappa = 7.8 \times 10^{-3}$ mm^2. Three different wetting phase saturations S_w (ratio of the combined surface of wetting clusters to that of the pore space): 0.83, 0.77, and 0.71, were experimentally obtained by simultaneously injecting two immiscible phases (*i.e.*, air and water; see Jiménez-Martínez et al., 2017). The dimensions of the saturation images used as TDS are 3292×2182 pixels, which yield a resolution of 0.04 mm per pixel. The images consist of binary data in which air clusters have zero value and water areas are flagged with one. The solid obstacles (grains) are always at the same location and are considered separately.

The static bulk saturations obtained experimentally are homogenous in both longitudinal and transverse directions. The size distribution of the non-wetting phase (air clusters) was previously analysed (Jiménez-Martínez et al., 2017). The gyrational radius of the air bubbles (also termed here air clusters indistinctly) was used as measure. The obtained distributions were in a good agreement with previous findings (Tallasktad et al., 2009), showing that desaturation (*i.e.,* increase in the air content) gives rise to a broader distribution of the air bubble sizes.

2.2. Multiple-point statistics at pore scale: simulations of phases distributions

The multiple point statistics (MPS) algorithm DeeSse (Straubhaar et al., 2020) was used to generate a set of stochastic simulations of the phases distributions for each saturation value by considering the corresponding TDS. The simulations are generated on a grid with the same dimensions as the TDS. The areas covered by the solid obstacles are masked at all simulations because their location and size remain constant in time. Since the geometry of the air and water phases is affected by surface tension processes at the contacts with the solid obstacles, the MPS algorithm needs to account for the position of the solid surface. This is accomplished by computing a distance to the surface of the solid obstacles and using it as secondary variable during the MPS simulation process. This distance is given together with the experimental data in the TDS and is used as conditioning data. Note also that for a better control of the proportion of air in the simulations, some isolated air pixels are randomly placed in the simulation grid, in order to nucleate some air clusters before running the MPS simulation.

The MPS simulation process is described in detail in Mariethoz et al. (2010). All pixels defining the simulation grid (except those defining the solid obstacles) are successively populated in a random order. For each pixel, the spatial patterns constituted by the locations and values of the binary variable and the distance to the solid obstacles for the already simulated pixels closest to the current location are retrieved. Next, the TDS is randomly scanned until the algorithm finds an acceptable match between the aforementioned pattern of conditioning data in the simulation grid and in the TDS for both variables. The value at the central pixel of the pattern is then copied from the TDS and pasted on the simulation grid. As the simulation progresses, the density of the informed pixels on the grid increases, which results in a smooth transition from wide to narrow patterns. Hence, large- and small-scale patterns are borrowed from the TDS, and each simulation shares the spatial statistics of the TDS. The three main parameters of the algorithm (the maximum number of neighbours, the maximum scanned fraction of the TDS, and the acceptance threshold for accepting matching patterns) have been adjusted by trial and error to obtain enough variability between simulations and an adequate reproduction of the geometry of air clusters. This aspect is discussed in detail below.

In this study, the geometric and statistical coherence between the simulations and the TDS is guaranteed by comparing the saturation de-

gree and a number of morphological descriptors of the air phase distribution and air clusters, such as (1) the statistical distribution (pdf) of the radii pores occupied by air, (2) the area and perimeter of the air clusters, (3) the major and minor axes lengths of a statistically equivalent ellipse fitting the air clusters (*i.e.*, a "shape comparison" to an equivalent ellipse with the same normalized second central moments as the air cluster), and (4) the orientation of the major axis of those ellipses with respect to the main flow direction. Global similarity and dissimilarity measures are also calculated. The similarity is measured by the geometric connectivity of the air phase. A standard 8-connectivity measure for air clusters was used, in which air pixels are connected if their edges or corners touch each other. Two adjoining "air" pixels are part of the same object if they are connected along the horizontal, vertical, or diagonal direction (Cheng et al., 2009). The dissimilarity between the TDS and the simulations is measured by simply subtracting the binary images and counting the pixels whose absolute difference is ≥ 1. A global connectivity measure, consisting of the proportion of water pixels that connect the inlet and the outlet of the domain, is computed for each simulation (*i.e.*, isolated water pixels/clusters are ignored in this case). Since connectivity plays a key role in flow and transport processes, these measures for the simulations are expected to be similar to that of the TDS. Moreover, the proportion of mismatching pixels between the simulation and the TDS is computed. This global measure of dissimilarity reports on the variability of the set of simulations compared to the TDS.

2.3. Fluid flow and solute transport modelling, mixing and reaction

A finite element model, developed with COMSOL Multiphysics®, was used to simulate fluid flow and solute transport through the porous medium. Solid obstacles and the non-wetting phase (air) were considered immobile and incompressible. The latter assumption is valid due to the low flow rates used and the rheology of the wetting phase, which result in capillary forces stronger than viscous forces. This prevents deformation and the displacement of air bubbles. The size of the finite elements is variable and always smaller than the pixel size (0.04 mm) to alleviate numerical instabilities. In addition, the mesh was refined at the interfaces between phases, and thus depends on the simulation or TDS (*i.e.*, the laboratory experiment) under analysis. On average, more than 600′000 thousand triangular and quadrilateral finite elements define each mesh. Numerical instabilities are further alleviated by means of a refine temporal discretization defined by a geometric progression with common ratio 1.02 and starting time increment 0.23 s. Overall, 600 time steps were used for solving a time span of 10′000 s.

For each saturation degree, a steady-state velocity field is assumed for simplicity. To that end, the set of Navier-Stokes equations, representing creeping flow with very low Reynolds number and viscous effects more important than inertial effects, is solved at the wetting phase (water), as follows:

$$\rho_w\left(\frac{\partial u}{\partial t}+(u\cdot\nabla)u\right)=-\nabla p+\mu_w\left(\nabla^2 u+\frac{1}{3}\nabla(\nabla\cdot u)\right)+f \quad (1)$$

$$\frac{\partial \rho_w}{\partial t}+\nabla\left(u\cdot\rho_w\right)=0 \quad (2)$$

where u [m·s^{-1}] is fluid velocity, p [kg·m^{-1}·s^{-2}] is fluid pressure, ρ_w [kg·m^{-3}] and μ_w [kg·m^{-1}·s^{-1}] are water density and dynamic viscosity, respectively, and f [kg·m^{-2}·s^{-2}] is the volumetric force term in the momentum equation. Values used in this study are ρ_w = 1′099 kg·m^{-3} and μ_w = 0.0372 kg·m^{-1}·s^{-1}. The volumetric force term f was set to zero for simplicity. For the particular case of creeping flow, both advective and gravity terms can be neglected. Under steady-state conditions and considering an incompressible fluid, the continuity Eq. (2) can be rewritten as $\nabla \bullet u = 0$. Therefore, the resulting creeping flow formulation is:

$$-\nabla p+\mu_w\cdot\nabla^2 u+f=0 \quad (3)$$

The partial differential Eq. (3) is constrained by boundary conditions representing constant flow rate q^* = 5.54·10^{-4} m^3·s^{-1} and constant pressure p^* = 0 kg·m^{-1}·s^{-2} at the inlet and outlet of the domain, respectively.

Table 1
Mean flow velocity ($\bar{u}$), Reynolds (Re) and Péclet (Pe) numbers for each saturation. q_{sat} denotes the prescribed flow rate at the inlet for the corresponding saturated case, in such a way that the Péclet number is the same as in the unsaturated counterpart.

S_w	$\bar{u}$ [m·s^{-1}]	Re [-]	Pe [-]	q_{sat} [m^3·s^{-1}]
0.83	1.28·10^{-5}	4.43·10^{-4}	4.75	7.56·10^{-4}
0.77	1.44·10^{-5}	4.99·10^{-4}	5.34	8.50·10^{-4}
0.71	1.67·10^{-5}	5.77·10^{-4}	6.18	9.83·10^{-4}

No-slip conditions were considered at the liquid-gas and liquid-solid interfaces, setting to zero the flow velocity along them. This assumption simplifies the workflow and reduces the computational effort, while its impact on transport processes is negligible (Guédon et al., 2019; Triadis et al., 2019).

Advection and diffusion processes were considered for the simulation of solute transport:

$$\frac{\partial c}{\partial t}=\nabla\cdot(D\nabla c)+u\cdot\nabla c \quad (4)$$

where c [mol·m^{-3}] is solute concentration and D [m^2·s^{-1}] is molecular diffusion (D = 10^{-9} m^2·s^{-1} in this study). A constant concentration (c^* = 1 mol·m^{-3}) was injected at the inlet. The mean fluid flow velocities ($\bar{u}$), and computed dimensionless numbers to characterize flow and transport, *i.e.*, Reynolds number: $Re=\rho_w\bar{u}a/\mu_w$, and Péclet number: $Pe=\bar{u}a^2/(2D\lambda)$, respectively, for each saturation are summarized in Table 1.

In this work, we evaluate the relative importance of dispersion, mixing and reaction. To that end, we analyse the geometry of the mixing zone and the reactivity within. The geometry of the mixing zone Ω_m (where $0 < c < 1$) is characterized by its area, S_m [m^2], defined as $\Omega_m = \{(x,y) \mid 0.02 < c(x,y) < 0.98$ mol·m$^{-3}\}$ to get rid of spurious numerical effects, and by the length Σ [m] of its centre line Γ, defined as the set of locations where c = 0.5 mol·m^{-3}. Γ can be interpreted as the interface between the resident and injected solutions, *i.e.,* the centre line of a diffuse interface. Reactions are often consequence of the miscibility between two solutions. In particular, mixing-driven reactions take place when the characteristic reaction time scale, t_r [s], is smaller than the characteristic advective time, $t_a=\lambda/\bar{u}$, also in [s]. In that case, the Damköhler number ($Da=t_a/t_r \gg 1$) is large and local reaction rates r [mol· m^{-3}·s^{-1}] can be computed from the measured concentration fields (de Simoni et al., 2005, 2007; Willmann et al., 2010):

$$r=\frac{2K}{\left(c^2+4K\right)^{3/2}}D\|\nabla c\|^2 \quad (5)$$

where K [mol^2·m^{-6}] is the equilibrium constant of the reaction (K = 10^{-2} mol^2·m^{-6} in this study). The upscaled reactivity, termed here global reaction rate R [mol·s^{-1}], is computed as the integral of the local reaction rates r over the mixing zone ($R=\int_{\Omega_m} dxdyr$). The integral of R over time is the total mass of reaction product, M_T [mol] (Jiménez-Martínez et al., 2015).

3. Results and discussion

3.1. Geometrical coherence

A total of 200 MPS equally likely simulations per saturation were generated that honour the saturation of the corresponding TDS with a tolerance ±0.02 (Figure S1, Supplementary Material). The simulations resemble the corresponding TDS well because multiple-point statistical patterns are properly inherited (Figure S2, Supplementary Material). Indeed, the locations of air clusters are different at all simulations (and different to those in the TDS). The simulations are dissimilar from the TDS, as measured by the fraction of "wet pixels" with different value (*e.g.*, air

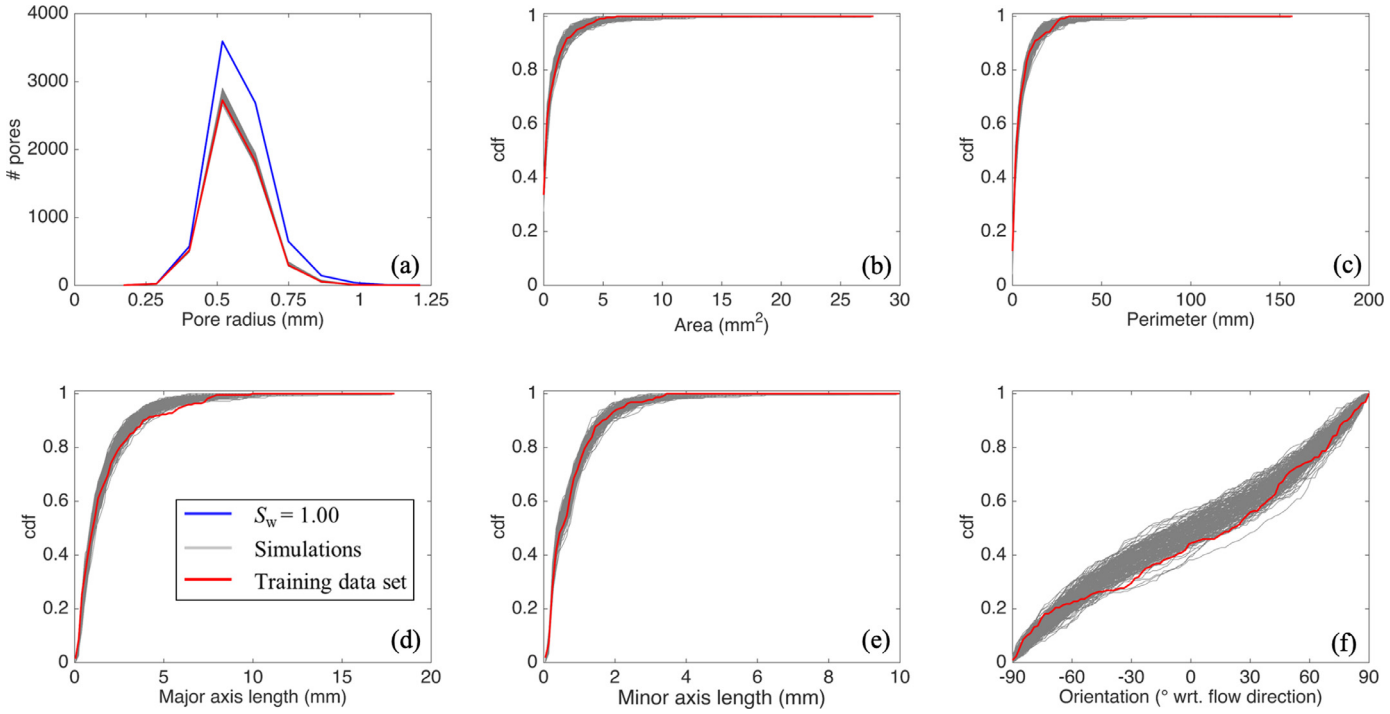

Fig. 1. Comparison between geometric descriptors of the simulated distributions of air clusters (grey lines) and those of the training data set for a saturation $S_w = 0.83$ (red line): unsaturated pore radii (a), cumulative distribution function (cdf) of the area (b) and perimeter (c) of the non-wetting clusters, cdfs of the major (d) and minor (e) axes lengths of area-equivalent ellipses fitting the non-wetting clusters, and cdfs of the orientation of air clusters with respect to the main flow direction in the flow and transport model (f). The blue line in panel (a) represents S_w =1.00 as a reference. (For interpretation of the references to color in this figure legend, the reader is referred to the web version of this article.)

in the simulation but water in the TDS or vice versa; note that the location of the solid obstacles is the same at the TDS and the simulations; see Figure S2, Supplementary Material). As expected, the differences between the TDS and the simulations increase with decreasing saturation because the air clusters are more prominent. However, the connectivity of the air phase in the TDS and the simulations is still similar, which corroborates the overall resemblance of the spatial patterns contained in the TDS. Additionally, the connectivity of the air phase decreases with increasing saturation (see Figure S3, Supplementary Material).

Fig. 1a displays the distribution of radii of saturated pores for a saturation $S_w = 0.83$. As observed, the similarity between the distributions attained with the TDS and with the simulations is striking. All distributions are centred around a mean pore radius $\sim$ 0.55 mm, *i.e.*, the non-wetting phase (air) does not occupy the largest pores (the average pore size $\lambda = 1.85$ mm). This is due to the desaturation of the experimental porous medium, caused by the simultaneous injection of both phases before reaching a final static bulk saturation (Jiménez-Martínez et al., 2017). The cumulative distribution functions (cdf) of area and perimeter of the simulated air clusters reproduce well those of the TDS (Fig. 1b, c). The cdfs of the major and minor axes lengths of an area-equivalent ellipse fitting the simulated air clusters also reproduce the corresponding ones of the TDS, although in the first case, simulated major lengths are slightly above the experimental observations (Fig. 1d, e). The comparison between the cdfs of orientation (inclination with respect to the main flow direction, from left to right) of air clusters indicates that the simulated air clusters mimic the experimental orientations with deviations smaller than 30° (Fig. 1f). The same analysis has been performed for saturations S_w = 0.77 and 0.71 and leads to identical qualitative conclusions (Figures S4 and S5, Supplementary Material).

With these analyses, it is ascertained that the simulations analogue to the training data sets because the simulated phases distributions (1) mimic the statistics of several morphological descriptors of the TDS with minimal deviations explained by the random nature of the simulation process, and (2) resemble the physics of multiphase flow processes in unsaturated media, in the sense that the simulated distributions of saturated pore radii are almost identical to those of the TDS. In short, MPS allows to extract the most information out of a costly, hardly repeatable and time-consuming laboratory experiment, which enables the analysis of the impact of phases distribution on mixing and reaction, evaluated next.

3.2. Impact of phases distribution on mixing

We randomly selected a subset of 10 simulations for each TDS and numerically solved flow and solute transport (see Section 2.3). Fig. 2 displays the spatial distribution of solute concentration for each TDS and two simulations. The visual inspection of the TDS and simulation outputs for a given saturation already reveals the impact of phases distribution on solute transport (*e.g.*, different spreading and development of distinct fingering patterns). This impact is best evaluated quantitatively, by means of solute mixing and chemical reaction descriptors.

A first measure of the impact of phase distribution on solute transport is given by the breakthrough curves (BTCs, Fig. 3), which report on solute spreading. The enhanced development of a fingering pattern causes earlier arrival times under unsaturated conditions through preferential flow paths, but more pronounced tailing, due to the existence of low velocity and even stagnation regions (Guédon et al., 2019), than in the saturated case (blue lines in Fig. 3) under identical *Pe* conditions. The development of fingers under unsaturated conditions drives the so-called anomalous transport or non-Fickian solute dispersion (Bromly and Hinz, 2004; Cortis and Berkowitz, 2004; Zoia et al., 2010; Guillon et al., 2013), whose effect in tailing is similar to that caused by aquifer heterogeneity (Carrera et al., 1998; Sanchez-Vila and Carrera, 2004; Alcolea et al., 2008; Silva et al., 2009). As observed, the tailing in the simulated BTCs is more pronounced than that in the corresponding TDS regardless of saturation. We attribute this disturbing

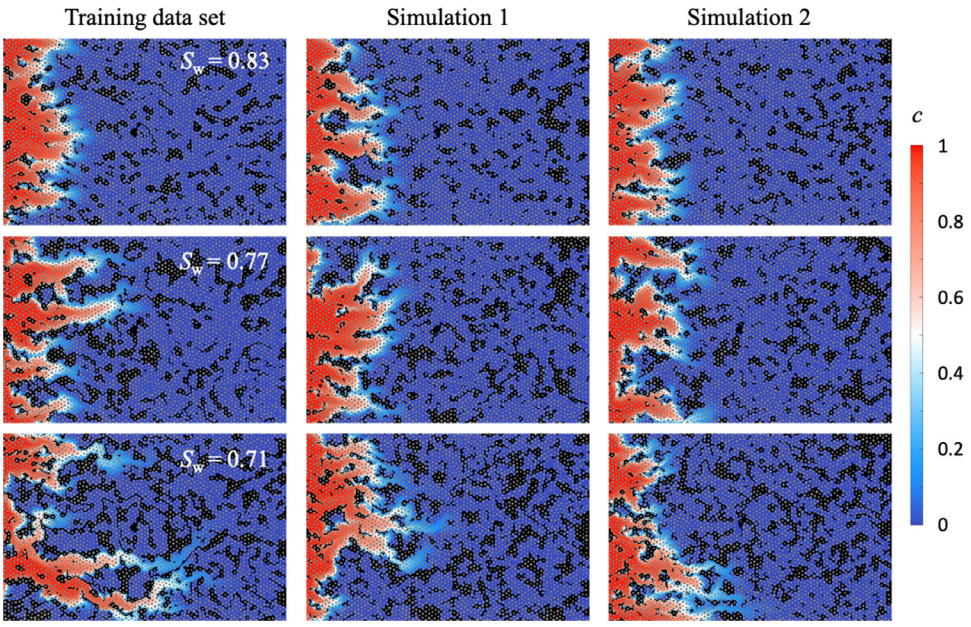

Fig. 2. Spatial distribution of solute concentration (c; blue to red colour map) at a common time step (t = 2190s, ~ 1/5 of the simulated period) for each TDS (*i.e.*, water saturation, S_w = 0.83, 0.77, and 0.71) and two simulations (air phase: black; solid obstacles: grey). The TDS and all corresponding simulations are carried under the same *Pe* (Table 1). (For interpretation of the references to color in this figure legend, the reader is referred to the web version of this article.)

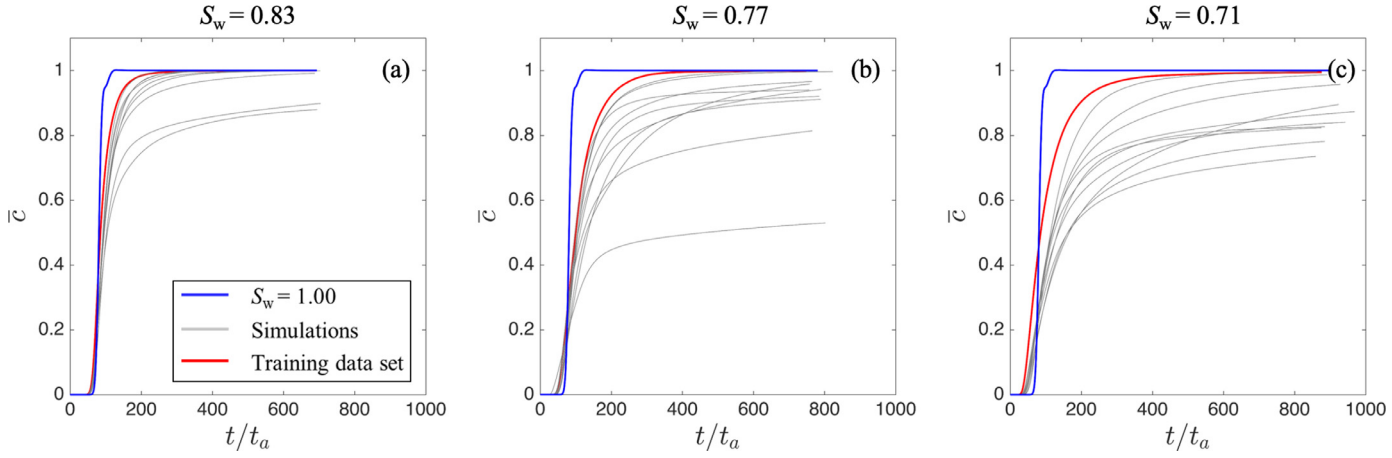

Fig. 3. Breakthrough curves (BTCs) measured at the outlet for fully saturated (S_w = 1, blue line) and unsaturated conditions: (a) S_w = 0.83, (b) S_w = 0.77, and (c) S_w = 0.71 (TDS: red line; simulations: grey lines). For each saturation, solute transport in the saturated counterpart was computed under identical *Pe* (Table 1). (For interpretation of the references to color in this figure legend, the reader is referred to the web version of this article.)

finding to small statistical differences between the TDS and the simulations, mainly in the orientation and major equivalent length of air clusters (Fig. 1d and f). Simulations are, indeed, noisier than the high-resolution and smooth TDS. Thus, they may contain a number of small air clusters leading to enhanced contact surfaces between mobile and immobile phases. As saturation decreases, the larger control of phases distribution (*i.e.*, the location of the air clusters) on fingers' development causes a general larger variability in the late time behaviour of the BTCs, and therefore in solute spreading. However, neither solute spreading nor the BTCs report on chemicals reactions within the system because reactivity depends on local fluctuations of solute concentration, *i.e.*, on solute mixing.

Spreading and mixing are coupled, *i.e.*, spreading enhances mixing and mixing smooths out concentration contrasts at close locations. The calculated concentration fields are used to compute the temporal evolution of the area of the mixing zone, S_m (Fig. 4). In the fully saturated cases, ran under the same *Pe* as the corresponding unsaturated case, an initial increase of the area of mixing is observed, followed by a Fickian scaling, $S_m \sim t^{1/2}$. The initial increase results from the pseudo-uniform development of small fingers (Figure S6, Supplementary Material). When early fingers merge by the action of molecular diffusion, mixing follows approximately a Fickian scaling (Le Borgne et al., 2013, 2015). In the unsaturated cases, an initial increase is also observed (although more pronounced, due to the development of more fingers than in the saturated case), followed by a temporal scaling larger than Fickian. This late-time effect is explained by enhanced fingering and a limited impact of molecular diffusion caused by the presence of air clusters (Jiménez-Martínez et al., 2015, 2017). The late-times scaling increases as saturation decreases (Fig. 4). In other words, mixing is enhanced as saturation decreases because the impact of heterogeneity introduced by the air clusters is larger (see also Figure S5, Supplementary Material). Note that, at long term, very small variability in the scaling is observed for the TDS and the corresponding simulations regardless of saturation. This could make one think that phase distribution controls only the early time behaviour of the mixing area, but not its final trend. While this is true in terms of late-time scaling, the final value of area of mixing largely depends on phases distribution, as discussed below.

A second descriptor of solute mixing is the length of the interface between the resident and the injected solutions, Σ (*i.e.*, the centre line of a diffusive interface Γ; Fig. 5). At early times of injection, Σ increases

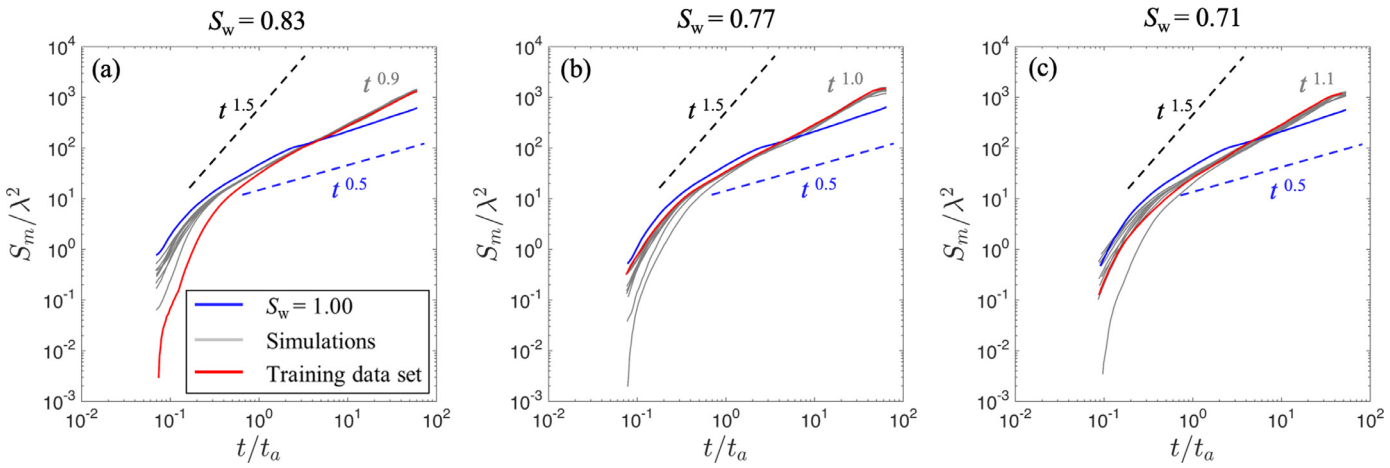

Fig. 4. Temporal evolution of the area of the mixing zone S_m for fully saturated ($S_w = 1$, blue line) and unsaturated conditions: (a) $S_w = 0.83$, (b) $S_w = 0.77$, and (c) $S_w = 0.71$ (TDS: red lines; simulations: grey lines). For each saturation, solute transport in the saturated counterpart was computed under identical *Pe* (Table 1). The blue dashed lines represent the Fickian behaviour. The grey insets contain the mean scaling of the unsaturated cases of both TDS and simulations. (For interpretation of the references to color in this figure legend, the reader is referred to the web version of this article.)

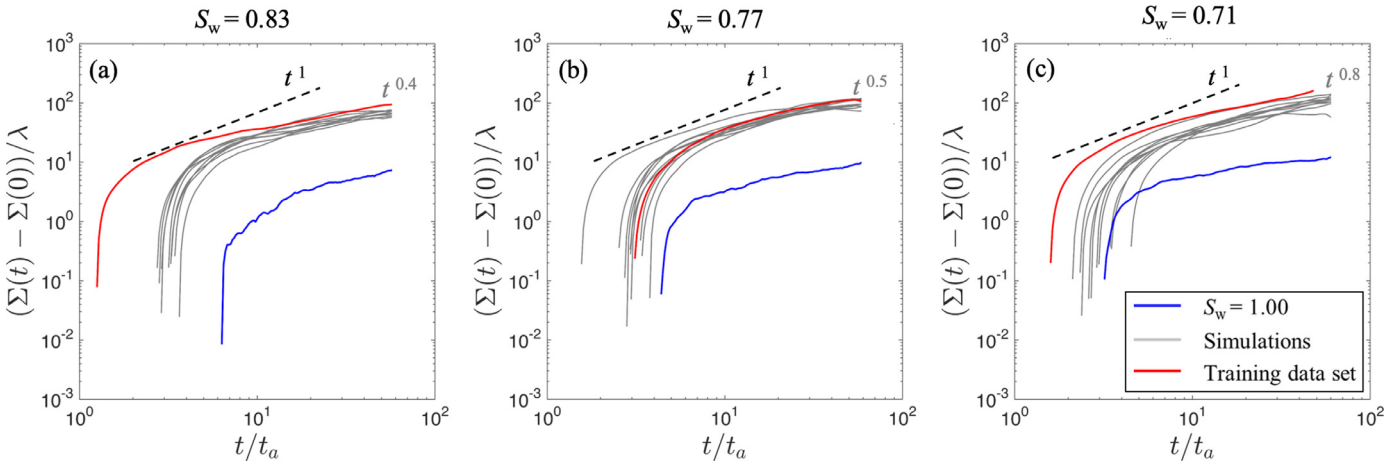

Fig. 5. Temporal evolution of the interface length $\Sigma(t) - \Sigma(0)$, where $\Sigma(0)$ is its initial value, for fully saturated ($S_w = 1$, blue line) and unsaturated conditions: (a) $S_w = 0.83$, (b) $S_w = 0.77$, and (c) $S_w = 0.71$ (TDS: red lines; simulations: grey lines). For each saturation, solute transport in the saturated counterpart was computed under identical *Pe* (Table 1). The grey insets contain the mean scaling of the unsaturated cases of both TDS and simulations. The black dashed lines represent linear scaling for reference. (For interpretation of the references to color in this figure legend, the reader is referred to the web version of this article.)

sharply regardless of saturation due to invasion of the mixing front, as observed in the experiments carried out by de Anna et al. (2014) and Jiménez-Martínez et al. (2015), amongst others. Under unsaturated conditions, the variability of the entry time is larger as saturation decreases because the amount and spatial distribution of air clusters near the inlet plays an important role. Instead, under saturated conditions, experimental observations indicate that Σ stabilizes at a plateau caused by the merging of fingers due to molecular diffusion (Jiménez-Martínez et al., 2015). Although a trend towards a plateau is observed, this was not the case in our simulations because the model length along the main flow direction is small and *Pe* is large. Instead, under unsaturated conditions, experimental observations reveal that Σ increases faster than linear due to enhanced fingering and does not reach a plateau until late times of system homogenization (de Barros et al., 2012). In fact, our simulations show both extremes and demonstrate the large impact of saturation on solute mixing. Contrary to the area of mixing presented above (Fig. 4), which largely depends on the type of experiment under analysis, the length of the interface between resident and injected solution displays a very large variability regardless of saturation. The variability in the temporal evolution of the interface length increases with decreasing saturation. This is explained by a larger control of the spatial distribution of air clusters on the deformation of the interface.

3.3. Impact of phases distribution on mixing-induced reactions

Concentration gradients within solute plumes control diffusive mass transfer and local reaction rates. The global reaction rate R, computed as the integral of the local reaction rates over the mixing zone, is significantly impacted by saturation (Fig. 6, a to c). Under fully saturated conditions, and after an initial increase, R decreases following a Fickian or diffusive decay ($R \sim t^{-1/2}$). This indicates that after the initial deformation of the invasive front, the coalescence of small fingers causes mass transfer to scale as a molecular diffusion process. Under unsaturated conditions, R increases initially in a similar manner and then decreases slower than under fully saturated conditions, or even keeps on increasing, depending on saturation. As expected, R increases with decreasing saturation (Jiménez-Martínez et al., 2015). The higher reaction rates observed at late times under unsaturated conditions translate directly into a larger mass of the reaction product, M_p, than in the fully saturated counterparts (Fig. 6, d to f).

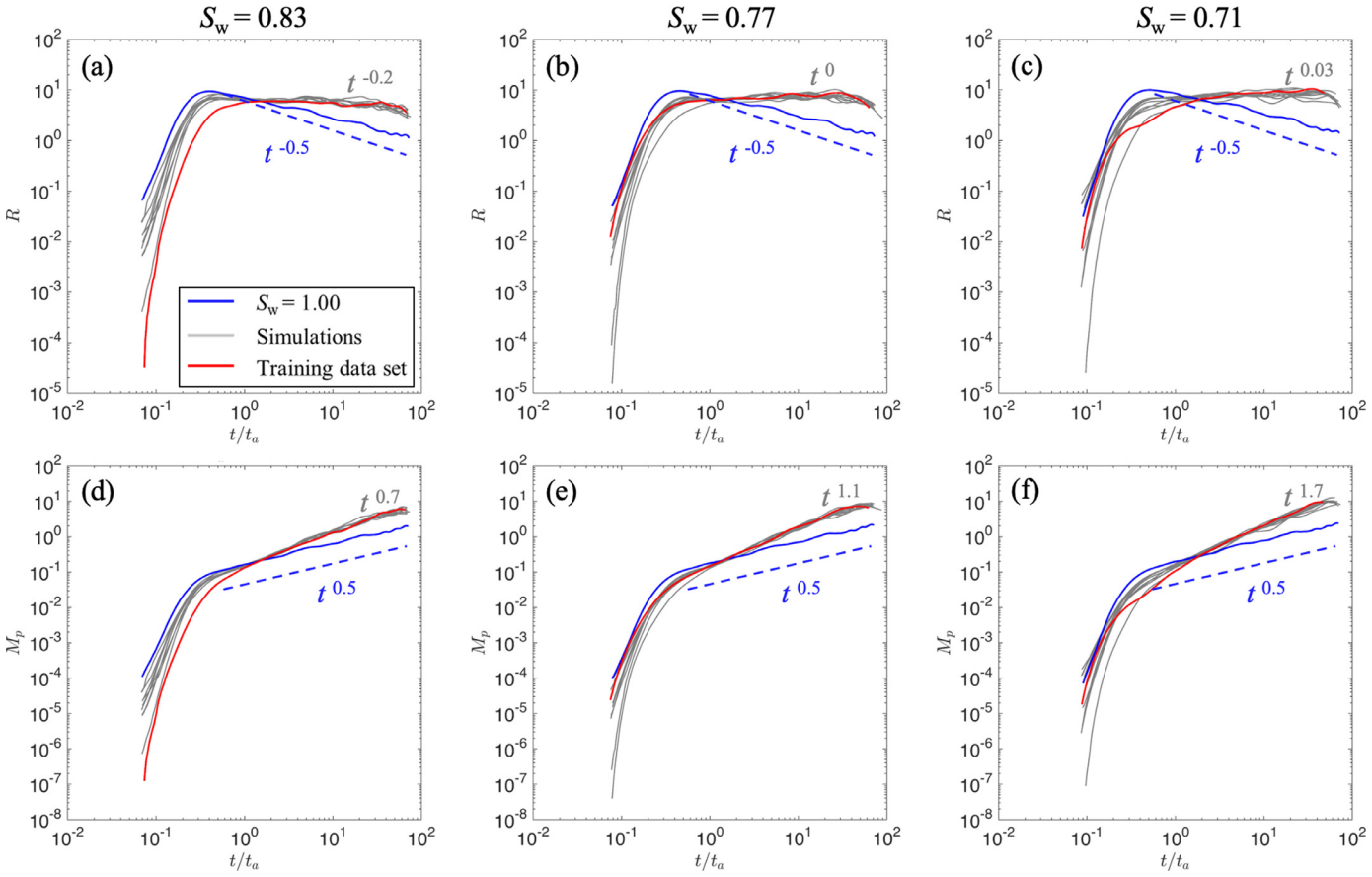

Fig. 6. Temporal evolution of the global reaction rate R for fully saturated ($S_w = 1$, blue line) and partially saturated conditions: (a) $S_w = 0.83$, (b) $S_w = 0.77$, and (c) $S_w = 0.71$ (TDS: red line; simulation: grey line). Mass of reaction product M_P for fully saturated ($S_w = 1$, blue line) and partially saturated conditions: (d) $S_w = 0.83$, (e) $S_w = 0.77$, and (f) $S_w = 0.71$ (TDS: red line; simulation: grey line). Note that transport in the saturated counterpart for each unsaturated case was computed under the same Pe as for unsaturated conditions. The blue dashed lines represent Fickian behaviour. The grey insets contain the mean scaling of the unsaturated cases of both TDS and simulations. (For interpretation of the references to color in this figure legend, the reader is referred to the web version of this article.)

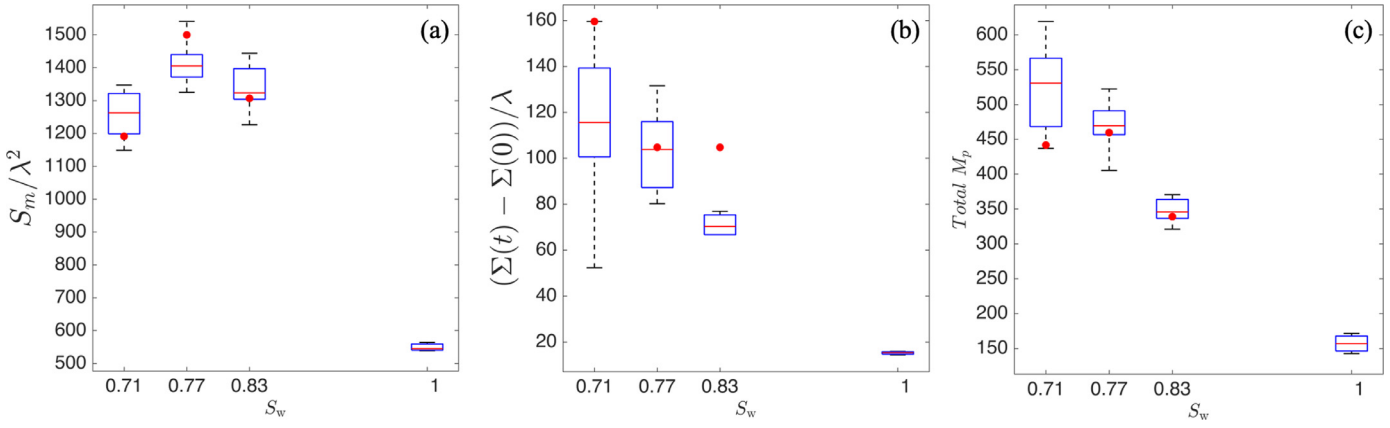

Fig. 7. Box and whisker plots of mixing and reaction descriptors at late times, prior to breakthrough (a) area of the mixing zone; (b) interface length; (c) total mass of reaction product M_T. The central mark (red lines) indicates the median and the bottom and top lines (blue) indicate the 25th and 75th quantiles, respectively. The wings of the box plot depict the minimum and the maximum values. The red dots represent the corresponding value of the TDS. Note that, for a given saturation, the value of the different simulations and of the TDS may correspond to different breakthrough times. (For interpretation of the references to color in this figure legend, the reader is referred to the web version of this article.)

The joint impact of saturation and phases distribution on mixing and reaction is best observed in Fig. 7, which displays the box and whisker plots of the final value of the analysed descriptors prior to breakthrough, including the area of the mixing zone, the interface length, and the total mass of reaction product. Saturation controls the topology of the system, which is dominated by the number and extent of the air clusters. Instead, phases distribution relates to the way the air clusters are distributed over the modelled domain. Both concepts are linked through entropy, which measures the degree of disorder or randomness of the system. It has been demonstrated that entropy increases as saturation de-

creases. However, entropy is not only controlled by saturation, but also by phases distribution, *i.e.*, similar entropies may be obtained for different saturations (Jiménez-Martínez and Negre, 2017). These authors also show that an increase of entropy also implies an enhanced "mixing capacity". While the final (prior to breakthrough) area of mixing increases down to a saturation of $S_w = 0.77$, this trend is inverted at the lowest saturation $S_w = 0.71$. In the case of the final value of the interface length, a general increase is observed as saturation decreases and a larger variability is also observed. The total mass (in mol) of the reaction product ($M_T = \int_{t_0}^{t_{BT}} M_p dt$) produced before breakthrough (t_{BT}) increases with decreasing saturation. Although a general positive correlation exists between interface length and area of mixing, these results evidence the larger control of the interface length on the total mass of reaction product. For the lowest saturation ($S_w = 0.71$), the presence of more and larger air clusters enhances the stretching and folding of the invasive front (Le Borgne et al., 2013, 2015), *i.e.*, the creation of concentration gradients, even for a smaller area of mixing than in under higher saturations. For low saturations, while the creation of interface is enhanced, the mixing can be "volume limited", *i.e.*, the presence of air clusters inhibits the growth of the mixing zone by molecular diffusion. As stated before for entropy, a similar total mass of reaction product may be obtained under different saturations (Fig. 7).

4. Concluding remarks

This work presents a novel methodology that combines a multiple point statistical method and transport simulations for the comprehensive analysis of the impact of saturation and phases distribution on solute dispersion, mixing and reaction in porous media. For a given saturation, the simulated phases distributions resemble the spatial patterns observed in the corresponding training data set (*i.e.*, an experimental image), as indicated by several geometrical and physical descriptors. In other words, simulations are analogues to experiments hardly repeatable in the laboratory. This enables further analyses.

A large impact of phases distribution on early arrival times and long-term tailings has been observed in the breakthrough curves regardless of saturation, with increasing variability as saturation decreases. The phases distribution at the inlet of the domain largely controls the early time evolution of the area of mixing and, particularly, of the interface length, which shows a larger variability and is controlled by the fingering pattern developed at early times of invasion of the solute front. The late time behaviour has been analysed both in absolute and relative terms (final value –before breakthrough– and temporal scaling). For a given saturation, small differences in the late-time temporal scaling of the area of mixing and interface length have been observed regardless of phases distribution. The impact of saturation is revealed by the different late-time scaling, which increases in both cases as saturation decreases, thus depicting a more pronounced non-Fickian behaviour. The joint impact of saturation and phases distribution is clearly observable in the final values of the area of mixing and interface length. Both generally increase as saturation decreases, an exception being the area of the mixing zone under the lowest saturation. In this case, mixing is inhibited by the limited accessibility of the injected solute to the resident liquid, which is hindered by the numerous isolated water clusters. A larger variability is observed in the final values of the interface length, indicating a larger control of phases distribution as saturation decreases.

The temporal evolution of the global reaction rate and the mass of reaction product (and, correspondingly, the total mass of reaction product), results from the interplay between mixing area and interface length. Thus, the behaviour at early times is the same one described above. By observing these magnitudes, we demonstrate a larger control of the interface length. The presence of air promotes the formation of interface length by stretching and folding the invasive front, thus enhancing the creation of concentration gradients and therefore of mass reaction product. In spite of the increasing of the late-time temporal scaling of global reaction rate and mass of reaction product with decreasing saturation, the heterogeneity introduced by phases distribution yields similar magnitudes of the total mass of reaction product for different saturations. In a nutshell, phases distribution controls the total mass of reaction product, while its late-time scaling is controlled by saturation.

Much remains to be done, both at pore and continuum scales. For instance, at continuum scale, the knowledge of the actual saturation distribution in unsaturated soils and the actual spatial distribution of hydraulic conductivity in aquifers is essential to reduce the uncertainty of the predictions the total mass of reaction product. The methodology presented here is general and allows further analyses with minimal changes in the model set-up. This allows to analyse numerically what is costly, hardly repeatable and time-consuming in the laboratory. This work is a step forward in the modelling of the joint impact of phases distribution and saturation in solute dispersion, mixing and reaction in unsaturated porous media.

Declaration of Competing Interest

The authors declare that they have no known competing financial interests or personal relationships that could have appeared to influence the work reported in this paper.

CRediT authorship contribution statement

Joaquín Jiménez-Martínez: Conceptualization, Methodology, Writing - review & editing. **Andrés Alcolea:** Conceptualization, Methodology, Writing - review & editing. **Julien A. Straubhaar:** Methodology, Writing - original draft. **Philippe Renard:** Methodology, Writing - review & editing.

Acknowledgements

JJM gratefully acknowledges the financial support from the Swiss National Science Foundation (SNF, grant Nr. 200021_178986). We thank the three anonymous reviewers whose valuable comments and suggestions help to improve the manuscript. We also acknowledge Andrés Valencia and Almudena Sánchez for the constructive discussions.

Supplementary materials

Supplementary material associated with this article can be found, in the online version, at doi:10.1016/j.advwatres.2020.103697.

References

Alcolea, A., Carrera, J., Medina, A., 2006. Pilot points method incorporating prior information for solving the groundwater flow inverse problem. Adv. Water Resour. 29 (11), 1678–1689.

Alcolea, A., Carrera, J., Medina, A., 2008. Regularized pilot points method for reproducing the effect of small scale variability: application to simulations of contaminant transport. J. Hydrol. 355, 76–90.

Bunsri, T., Sivakumar, M., Hagare, D., 2008. Influence of dispersion on transport of tracer through unsaturated porous media. J. Appl. Fluid Mech. 1 (2), 37–44.

Bromly, M., Hinz, C., 2004. Non-Fickian transport in homogeneous unsaturated repacked sand. Water Resour. Res. 40, W07402. https://doi.org/10.1029/2003WR002579.

Carrera, J., Sanchez-Vila, X., Benet, I., Medina, A., Galarza, G., Guimerà, J., 1998. On matrix diffusion: formulations, solution methods and qualitative effects. Hydrogeol. J. 6, 178–190.

Cheng, C.C., Peng, G.J., Hwang, W.L., 2009. Pixel connectivity. IEEE Trans. Image Process. 18 (1), 52–62. https://doi.org/10.1109/TIP.2008.2007067.

Chiogna, G., Hochstetler, D., Bellin, A., Kitanidis, P., Rolle, M., 2012. Mixing, entropy and reactive solute transport. Geophys. Res. Lett. 39. https://doi.org/10.1029/2012GL053295.

Comunian, A., Renard, P., Straubhaar, J., 2012. 3D multiple-point statistics simulation using 2D training images. Comput. Geosci. 40, 49–65.

Cortis, A., Berkowitz, B., 2004. Anomalous transport in classical soil and sand columns. Soil Sci. Soc. Am. J. 68, 1539–1548.

de Anna, P., Jimenez-Martinez, J., Tabuteau, H., Turuban, R., Le Borgne, T., Derrien, M., Méheust, Y., 2014. Mixing and reaction kinetics in porous media: an experimental pore scale quantification. Environ. Sci. Technol. 48, 508–516.

de Barros, F., Dentz, M., Koch, J., Nowak, W., 2012. Flow topology and scalar mixing in spatially heterogeneous flow field. Geophys. Res. Lett. 39, L08404. https://doi.org/10.1029/2012GL051302.

de Gennes, P.G., 1983. Hydrodynamic dispersion in unsaturated porous media. J. Fluid Mech. 136, 189–200.
de Simoni, M., Carrera, J., Sanchez-Vila, X., Guadagnini, A., 2005. A procedure for the solution of multicomponent reactive transport problems. Water Resour. Res. 41, W11410. https://doi.org/10.1029/2005WR004056.
de Simoni, M., Sanchez-Vila, X., Carrera, J., Saaltink, M., 2007. A mixing ratios-based formulation for multicomponent reactive transport. Water Resour. Res. 43, W07419. https://doi.org/10.1029/2006WR005256.
De Smedt, F., Wierenga, P.J., 1984. Solute transfer through columns of glass beads. Water Resour. Res. 20 (2), 225–232.
Dentz, M., Le Borgne, T., Englert, A., Bijeljic, B., 2011. Mixing, spreading and reaction in heterogeneous media: a brief review. J. Contam. Hydrol. 120-121, 1–17 120-121.
Feng, J., Teng, Q., He, X., Wu, X., 2018. Accelerating multi-point statistics reconstruction method for porous media via deep learning. Acta Mater. 159, 296–308.
Fluhler, H., Durner, W., Flury, M., 1996. Lateral solute mixing processes-a key for understanding field-scale transpor of water and solutes. Geoderma 70, 165–183.
Gouet-Kaplan, M., Berkowitz, B., 2011. Measurements of interactions between resident and infiltrating water in a lattice micromodel. Vadose Zone J. 10 (2), 624–633.
Guédon, G.R., Inzoli, F., Riva, M., Guadagnini, A., 2019. Pore-scale velocities in three--dimensional porous materials with trapped immiscible fluid. Phys. Rev. E 100 (4), 043101.
Guillon, V., Fleury, M., Bauer, D., Neel, M., 2013. Superdispersion in homogeneous unsaturated porous media using NMR propagators. Phys. Rev. E 87, 043007.
Haga, D., Niibori, Y., Chida, T., 1999. Hydrodynamic dispersion and mass transfer in unsaturated flow. Water Resour. Res. 35, 1065–1077.
Hajizadeh, A., Safekordi, A., Farhadpour, F.A., 2011. A multiple-point statistics algorithm for 3D pore space reconstruction from 2D images. Adv. Water Resour. 34 (10), 1256–1267.
Hasanabadi, A., Baniassadi, M., Abrinia, K., Safdari, M., Garmestani, H., 2016. Efficient three-phase reconstruction of heterogeneous material from 2D cross-sections via phase-recovery algorithm. J. Microsc. 264 (3), 384–393.
Jiménez-Martínez, J., de Anna, P., Tabuteau, H., Turuban, R., Le Borgne, T., Méheust, Y., 2015. Pore scale mechanisms for the enhancement of mixing in unsaturated porous media and implications for chemical reactions. Geophys. Res. Lett. 42, 5316–5324 10.1002/ 2015GL064513.
Jiménez-Martínez, J., Le Borgne, T., Tabuteau, H., Méheust, Y., 2017. Impact of saturation on dispersion and mixing in porous media: photo-bleaching pulse injection experiments and shear-enhanced mixing model. Water Resour. Res. https://doi.org/10.1002/2016WR019849.
Jiménez-Martínez, J., Negre, C.F.A., 2017. Eigenvector centrality for geometric and topological characterization of porous media. Phys. Rev. E 96, 013310. https://doi.org/10.1103/PhysRevE.96.013310.
Jougnot, D., Jiménez-Martínez, J., Legendre, R., Le Borgne, T., Méheust, Y., Linde, N., 2018. Impact of small-scale saline tracer heterogeneity on electrical resistivity monitoring in fully and partially saturated porous media: insights from geoelectrical milli-fluidic experiments. Adv. Water Resour. 10.1016/j.advwatres.2018.01.014.
Kapetas, L., Dror, I., Berkowitz, B., 2014. Evidence of preferential path formation and path memory effect during successive infiltration and drainage cycles in uniform sand columns. J. Contam. Hydrol. 165, 1–10.
Karadimitriou, N.K., Joekar-Niasar, V., Babaei, M., Shore, C.A., 2016. Critical role of the immobile zone in non-Fickian two-phase transport: a new paradigm. Environ. Sci. Technol. 50, 4384–4392.
Le Borgne, T., Dentz, M., Villermaux, E., 2013. Stretching, coalescence and mixing in porous media. Phys. Rev. Lett. 110, 204501.
Le Borgne, T., Dentz, M., Villermaux, E., 2015. The lamellar description of mixing in porous media. J. Fluid Mech. 770, 458–498.
Maraqa, M., Wallace, R., Voice, T., 1997. Effects of a degree of water saturation on dispersivity and immobile water in sandy soil columns. J. Contam. Hydrol. 25, 199–218.
Mariethoz, G., Renard, P., 2010. Reconstruction of incomplete data sets or images using direct sampling. Math. Geosci. 42 245e268.
Matsubayashi, U., Devkota, L.P., Takagi, F., 1997. Characteristics of the dispersion coefficient in miscible displacement through a glass beads medium. J. Hydrol. 192 (1–4), 51–64.
Nutzmann, G., Maciejewski, S., Joswig, K., 2002. Estimation of water saturation dependence of dispersion in unsaturated porous media: experiments and modelling analysis. J. Hydrol. 25, 565–576.
Padilla, I.Y., Yeh, T.C.J., Conklin, M.H., 1999. The effect of water content on solute transport in unsaturated porous media. Water Resour. Res. 35, 3303–3313.
Persson, M., Haridy, S., Olsson, J., Wendt, J., 2005. Solute transport dynamics by high-resolution dye tracer experiments- Image analysis and time moments. Vadose Zone J. 4, 856–865.
Raoof, A., Hassanizadeh, S.M., 2013. Saturation-dependent solute dispersivity in porous media: pore-scale processes. Water Resour. Res. 49, 1943–1951. https://doi.org/10.1002/wrcr.20152.
Roberts, A.P., 1997. Statistical reconstruction of three-dimensional porous media from two-dimensional images. Phys. Rev. E 56 3203e3212.
Rozman, M.G., Utz, M., 2001. Efficient reconstruction of multiphase morphologies from correlation functions. Phys. Rev. E 63, 066701.
Sanchez-Vila, X., Carrera, J., 2004. On the striking similarity between the moments of break-through curves for a heterogeneous medium and a homogeneous medium with a matrix diffusion term. J. Hydrol. 294 (1–3), 164–175.
Sato, T., Tanahashi, H., Loáiciga, H.A., 2003. Solute dispersion in a variably saturated sand. Water Resour. Res. 39 (6), 1155. https://doi.org/10.1029/2002WR001649.
Silva, O., Carrera, J., Kumar, S., Dentz, M., Alcolea, A., Willmann, M., 2009. A general real-time formulation for multi-rate mass transfer problems. Hydrol. Earth Syst. Sci. 13, 1399–1411.
Straubhaar, J., Renard, P., Chugunova, T., 2020. Multiple-point statistics using multi-resolution images. Stoch. Environ. Res. Risk Assess. 34, 251–273.
Tahmasebi, P., 2018. Accurate modeling and evaluation of microstructures in complex materials. Phys. Rev. E 97, 023307.
Tahmasebi, P., Sahimi, M., 2013. Cross-correlation function for accurate reconstruction of heterogeneous media. Phys. Rev. Lett. 110, 078002.
Tallakstad, K.T., Løvoll, H.A., Knudsen, G., Ramstad, T., Flekkøy, E.G., Måløy, K.J., 2009. Steady-state, simultaneous two-phase flow in porous media: an experimental study. Phys. Rev. E 80, 036308.
Toride, N., Inoue, M., Leij, F.J., 2003. Hydrodynamic dispersion in an unsaturated dune sand. Soil Sci. Soc. Am. J. 67, 703–712.
Triadis, D., Jiang, F., Bolster, D., 2019. Anomalous dispersion in pore-scale simulations of two-phase flow. Trans. Porous Med. 126 (2), 337–353.
Ursino, N., Gimmi, T., Fluhler, H., 2001. Dilution of non- reactive tracers in variably saturated sandy structures. Adv. Water Res. 24, 877–885.
Vanderborght, J., et al., 2001. Overview of inert tracer experiments in key Belgian soil types: relation between transport and soil morphological an hydraulic properties. Water Resour. Res. 37 (12), 2837–2888.
Willmann, M., Carrera, J., Sanchez-Vila, X., Silva, O., Dentz, M., 2010. Coupling of mass transfer and reactive transport for non-linear reactions in heterogeneous media. Water Resour. Res. 46, W07512. https://doi.org/10.1029/2009WR007739.
Yeong, C.L.Y., Torquato, S., 1998. Reconstructing random media. Phys. Rev. E 57, 495e506.
Zoia, A., Neel, M.-.C., Cortis, A., 2010. Continuous-time random-walk model of transport in variably saturated heterogeneous porous media. Phys. Rev. E 81, 031104.